4-2022

Novel Damage Index-Based Rapid Evaluation of Civil Infrastructure Subsurface Defects Using Thermography Analytics

Tianjie Zhang
Boise State University

Md Asif Rahman
Boise State University

Alex Peterson
Boise State University

Yang Lu
Boise State University

infrastructures

MDPI

Article

Novel Damage Index-Based Rapid Evaluation of Civil Infrastructure Subsurface Defects Using Thermography Analytics

Tianjie Zhang, Md Asif Rahman, Alex Peterson and Yang Lu *

Department of Civil Engineering, Boise State University, Boise, ID 83725-2060, USA; tjzhang@u.boisestate.edu (T.Z.); mdasifrahman@u.boisestate.edu (M.A.R.); alexpeterson841@u.boisestate.edu (A.P.)

* Correspondence: yanglufrank@boisestate.edu; Tel.: +1-(208)-426-3783

Abstract: The qualitative measurement is a common practice in infrastructure condition inspection when using Infrared Thermography (IRT), as it can effectively locate the defected area non-destructively and non-contact. However, a quantitative evaluation becomes more significant because it can help decision makers figure out specific compensation plans to deal with defects. In this work, an IRT-based novel damage index, damage density, was proposed to quantify the significance of subsurface defects. This index is extracted from IR images using our thermography analytics framework. The proposed framework includes thermal image processing, defect edge detection, and thermal gradient map calculations. A modified root mean square error (mRMSE), which is a novel modification to the existing RMSE, was compared to evaluate the performance of image processing methods. The results show that the histogram equalization performs better than the other methods in the image processing part as the mRMSE is the lowest among them. The Pearson correlation coefficient between the developed index and the volume of subsurface defects is 0.94, which indicates a positive linear relationship between them. Thus, the proposed damage index can be used to guide the engineering practices and maintenance decisions for the subsurface determination in the civil infrastructure.

Keywords: thermography analytics; subsurface defect; damage density; image processing

Citation: Zhang, T.; Rahman, M.A.; Peterson, A.; Lu, Y. Novel Damage Index-Based Rapid Evaluation of Civil Infrastructure Subsurface Defects Using Thermography Analytics. *Infrastructures* **2022**, *7*, 55. https://doi.org/10.3390/infrastructures7040055

Academic Editor: Alireza Sassani

Received: 28 February 2022
Accepted: 5 April 2022
Published: 8 April 2022

1. Introduction

Civil infrastructure, such as bridges and concrete pavement, requires maintenance to ensure safety and serviceability [1]. Even though concrete is inherently a durable material, civil infrastructures are susceptible to time-dependent deteriorations due to their exposure to various degradation mechanisms such as abrasion, moisture cycles, corrosion of reinforcements, and so on [2,3]. Particularly, subsurface deteriorations are invisible through visual inspection until the defects convert into a severe condition [4]. However, these kinds of subsurface defects may cause serious safety problems, including strength reduction, corrosion of the reinforcing rebar, and even structural failure.

To address this problem, the inspection of the civil infrastructure condition should gather chronological data, indicating the existence of the subsurface delamination and defects [5]. The traditional visual inspection method has been widely used in the past few decades. However, it is often time-consuming, labor-intensive, and difficult to detect subsurface deteriorations [6]. Therefore, Non-Destructive Testing (NDT) is becoming an attractive and fast approach to monitoring concrete conditions. Among many NDT methods, infrared thermography (IRT) is becoming even more popular in the fields of civil infrastructure damage detection, mainly due to its non-contact character, which includes two significant advantages: preventing the object from any alteration and keeping engineers away from any potential hazards [7–10]. The short detection time and qualitative evaluation of subsurface delamination are also significant advantages of the IRT technique [4]. The two main methods used in conducting an IRT test are passive thermography and active

thermography. The passive infrared thermography approach involves collecting radiated energy from the bridge, which does not generate electromagnetic energy [11]. The active thermography approach integrates infrared imaging with external heating. When the surface is heated, the heat will diffuse differently through delamination and the non-defect area leading to a heat convergence, which could be easily captured by an IR camera. Thus, it turns out to be a more effective method for inspecting the near-surface region [12,13].

The temperature spans in the infrared thermal image are considered the subsurface defects in concrete because of the difference between the thermal performance of concrete and delamination caused by the uneven distribution of heat [14]. The quick and effective inspection of these temperature differences is of prime concern of the engineers. Thus, to build an image-processing method using the IRT to extract the defected areas is badly needed to detect the subsurface delamination automatically. Due to the availability of low-cost and reliable imaging devices, a lot of infrared thermal image processing methods were developed to help decision makers quickly identify a defect's location and area under an automated feature. Changhang Xu proposed an infrared image processing framework based on a superpixel algorithm to inspect cracks [15]. Seungju Lee used a threshold value classification method to segment defects from an STS304 Reference Specimen and used an RMSE value as an evaluation metric when applying different filtering methods. However, the RMSE index only evaluates the prediction accuracy of the defects' area [16]. Chongsheng Cheng proposed a temperature-gradient-based level set method to detect the edges for defects segmentation and showed a better performance than the well-accepted k-means method [17]. Other methods such as K-means [1], region growing approach [18], and semantic segmentation [19] are also being used widely in defect detection.

Among many studies, most of them only focused on the area detecting accuracy of the subsurface defects [1,20]. The accuracy of defects' area evaluation is used as an index to determine the effectiveness of the IR thermal processing method they applied [21,22]. However, in field tests, the most interesting index for an engineer is to quantify how severe the damage is. In addition to the area, the thickness of defects also plays an essential role in a concrete's damage intensity while it has always been ignored. It is because the thermography is two-dimensional. Thus, the thickness is difficult to extract from an image. However, Slawomir Grys's work shows that subsurface defects with different depths and thicknesses have different visualization in IR images [23]. A numerical correlation between the crack profile and the crack temperature gradient was also found using a real-time thermal imaging-based system [8]. These findings identify that the information on the thickness of subsurface delamination can also be extracted from the IR image.

Thus, this paper aimed to propose a novel damage index which would depict the significance and distribution of subsurface defects in concrete both quantitatively and precisely through thermography analysis. It would take the defects' thickness into consideration. Therefore, a higher accuracy in damage condition prediction would be realized, compared to previous research, which only focused on the subsurface defects' area. To do this, an IRT-based damage density calculation framework was presented. First, the subsurface delamination was segmented by comparing and applying different infrared thermal image processing methods. A modified root mean square error (mRMSE) was selected to evaluate the performance, and the best performed one was chosen. Second, based on the segmented image, the damage index was calculated through edge detection and thermal image gradient map construction. Finally, the relationship between the damage index and volume of defects was evaluated based on lab tests. This relationship can show the correlation between the damage index and damage condition of the infrastructure because the volume of defects is generally related to the damage intensity in the detected concrete sample.

2. Materials and Methods

2.1. Damage Density

The qualitative measure is a common practice in infrastructure condition inspection field because an automated detection of the delamination can help engineers quickly locate

the defected area. However, an objective quantitative assessment is needed to meet the engineers' expectations. The engineers in this way can know how severe the damage is in the inspecting infrastructure depending on the quantitative evaluation, and can figure out some specific compensation plans to deal with the defects. To evaluate the significance of subsurface defects, several studies demonstrated that the area or perimeter of a subsurface defect detected by an IR camera could be used to quantitatively represent this defect [1,20]. However, the thickness of the defect was kept out of consideration while it actually would play an essential role in the concrete's damage intensity.

If the defect is more severe in its thickness, the contrast between the defect and the sound area would be sharper, which means the gradient around the edge of the defect becomes larger. Thus, in this work, the gradient of the detected deterioration area was used to represent the severe degree of the deterioration. A conception, damage density, was proposed to quantitatively depict the damage condition in an area. The damage density can be influenced by the total area of defects and the severe degree of each defect. Thus, a definition of damage density was proposed using the following Equation (1):

$$\rho_d = \frac{\sum_n^{i=1} \overline{\nabla}_i \hat{A}_i}{A} \tag{1}$$

where ρ_d is the damage density, A is the size of the overall IR image, which is equal to the thermal sensor resolution (640 × 512 pixels), $\hat{A}_i$ is the area of the ith defect detected in the IR image using the image processing method as presented in this study, $\overline{\nabla}_i$ is the mean gradient of the edge of the ith defect, n is the number of the total defects in a shot.

In Equation (1), if the damage density is 0, it means there is no delamination in the detected area. For each pixel in a normalized IR image, according to Equation (7), the theoretical largest gradient is $\sqrt{2}$. Thus, there exists a largest value $\sqrt{2}$ for the damage density, which means the detected area is destroyed most severely.

The damage density is a relatively integrated description of the significance and distribution of the delamination over the detected infrastructure. It quantifies the significance of subsurface defects more precisely, as more information was included in this index than only the area of the defects.

Damage density is calculated based on the proposed thermography analysis. In this work, a calculation framework was proposed as shown in Figure 1.

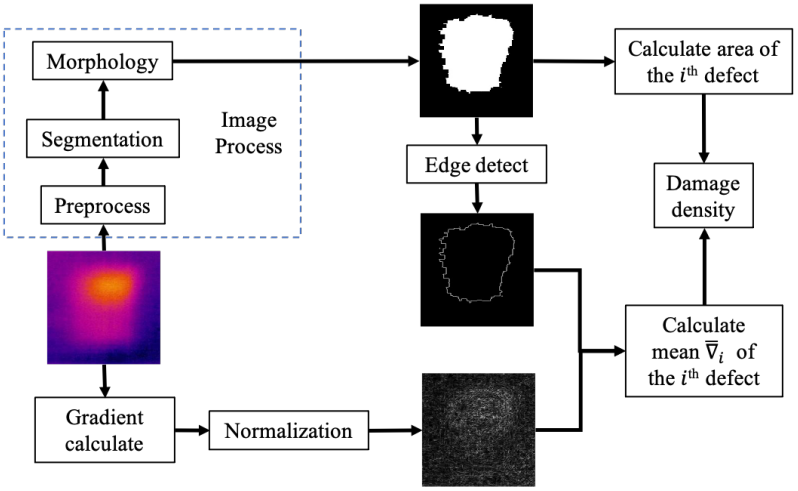

Figure 1. The diagram of the proposed framework.

At first, a proposed IR image processing method was used to segment the defects in order to obtain a predicted area $\hat{A}_i$ of the ith defect. The image processing method for automatic defect detection in this work includes image preprocessing, segmentation, and morphology.

Temperatures on the concrete surface were acquired using the FLIR Duo Pro R 640 thermal imager. Then, through the software FLIR ResearchIR MAX, the temperature files were converted to thermal images. The ROI (Region of Interest) was cropped from the thermal image. At the same time, the pixels included in the crop line could be counted, which can be used to calculate the scale between the real size and the image size.

Because of the noise and low-temperature contrast between the target and non-defect areas, preprocessing was recommended before image segmentation. Three kinds of filtering (mean, Log, Gaussian), and two image enhancement methods (contrast adjustment, histogram equalization) were introduced as preprocessing methods to denoise and enhance color contrast and were compared to choose the best suit one as the preprocessing part in the image processing procedure. Filtering is a technique for modifying or enhancing an image by sharping some features or removing random noise in a raw image. Mean, Log, and Gaussian are three different templates of filtering. Contrast adjustment is a way to remap image intensity values to the full display range. In this work, the gray level was remapped from [0.4, 0.7] to [0, 1], converting from a whole gray level to a sharper range which also contains the defects' information but less background noise. Histogram equalization can adjust the intensity values of image pixels automatically. It involves transforming the intensity values so that the histogram of the output image approximately matches a specified histogram.

After using the best performed preprocess method, the image was segmented by a modified OTSU algorithm. OTSU algorithm utilizes the variance in the gray-level distribution to calculate the optimal threshold value. It uses this optimal threshold to divide the image pixels into two parts: target (subsurface defect area) and background (non-defect areas). This algorithm can choose the threshold to maximize the between-part variance and minimize within-part variance [24,25]. However, the distribution of IR image gray-level histogram is skewed heavily. Compared to the mean, the median is a robust statistic value as a center metric in a skewed distribution. The original OTSU algorithm can be appropriately used in symmetric distribution because it uses the mean as its center metric. Thus, the mean was replaced by median in the OTSU algorithm to find the optimal threshold value in images after those are preprocessed. The modified OTSU algorithm can be described as follows.

Suppose the intensity of a gray-level histogram is expressed in L gray levels $[0, 1, \ldots, L-1]$. Assume the number of pixels in the ith level is n_i. The possibility of pixels in ith level is calculated by Equation (2) [25]:

$$p_i = \frac{n_i}{\sum_{L-1}^{i=0} n_i} \tag{2}$$

The probability of the target part p_1 and the probability of the background part p_2 can be calculated by Equations (3) and (4):

$$P_1 = \sum_{i=0}^{u} p_i \tag{3}$$

$$P_2 = \sum_{i=u+1}^{L-1} p_i \tag{4}$$

After the median values M_1, M_2, and M_T in P_1, P_2, and the whole image were calculated, respectively, the between-class variance δ^2 can be calculated by Equation (5):

$$\delta^2 = P_1(M_T - M_1)^2 + P_2(M_T - M_2)^2 \tag{5}$$

Finally, according to Equation (6), the optimal threshold u^* can be calculated when the between-class variance obtains the largest value:

$$u^* = argmax(\sigma^2_{0 \le u \le L-1}) \tag{6}$$

After segmentation, the image closing operation was introduced in the binary image to work as a second denoising. The morphological closing is defined as a dilation followed by an erosion in the field of image processing. It is because after segmentation, the defects may

be separated into several pieces because of the non-uniform distribution of temperature on the concrete surface or the uneven material mix during the sample casting. To obtain complete defect information, the separated pixels representing one defect should be linked together. Closing can remove small dark spots and connect small bright cracks. Thus, closing is a proper operational method for this task [15].

The gradient of each element in matrix of the original image can be calculated using Equation (7):

$$\nabla_{i,j} = (\frac{a_{i+1,j} - a_{i-1,j}}{2} i, \frac{a_{i,j+1} - a_{i,j-1}}{2} j) \quad (7)$$

where $\nabla_{i,j}$ is the gradient for the element $a_{i,j}$, which is located in the row i, column j of a matrix.

A gradient map of the raw image was calculated using Equation (7). Then, the gradient map was normalized to make the gradient in a same scale.

The raw image is converted to a binary image after using the proposed image processing method. In the binary image, the detected subsurface defects of the target area are marked as 1 (white), while the non-defect areas are marked as 0 (black). When calculating the gradient of this binary image, only the boundary of the defects would have values rather than zero because only the boundary has a gradient in the binarized picture. Thus, in this way, the edge of the target delamination can be located.

Depending on the segmented result, the area of the ith defects can be counted. The edge location from the segmented defects was used in the normalized gradient map to calculate the mean gradient $\overline{\nabla}_i$ of the ith defects. Finally, the area and the mean gradient were used according to the Equation (1) to obtain the damage density from the detected concrete part.

2.2. Samples

Eight specimens were modeled in this work. All the specimens were composed of cement (33.5%), sand (54.4%), and water (12.1%). The water/cement ratio (W/C) was fixed at 36.1%. The size of the concrete beam was 150 mm × 150 mm × 600 mm. Generally, the condition of in situ detection was more complex than in lab. The threshold for each subsurface defect should be tested because different kinds of subsurface delamination had different contrasts compared with the background in IR images. Applying the damage density framework to a field environment is challenging. Thus, subsurface voids became the main research purpose in this work. In order to mimic the subsurface voids of real civil infrastructure, various sizes, depths, and shapes of Styrofoam blocks were introduced in the concrete sample as shown in Figure 2.

This is because the Styrofoam's thermal conductivity (0.027 W/m °C) is close to the air (0.024 W/m °C). Another reason is that casting a hole internally in the concrete beam is difficult, and it would be easier to use the Styrofoam inside of the concrete beam while casting it in the cement-concrete lab. The sizes of these defects are described in Table 1. All the defects were embedded at a depth of 5 mm from the heating surface. In field detection, the voids inside concrete will not purely consist of 'air' voids as moisture and dust would also be parts of the voids. Moreover, the shapes of the voids are irregular. However, the main task in this work is to figure out the usability of the damage density index, so the voids were treated as cuboid shapes and purely consisted of air.

The IR analytics sensitivity is dependent on the contrast between defect (target) and concrete. The thermal property contrast between air and concrete is significantly larger than the contrast between Styrofoam and concrete. Thus, our lab setup simulates a more complex situation of the test design, which means subsurface voids detection in the field is much easier implementation than our lab setup scenario.

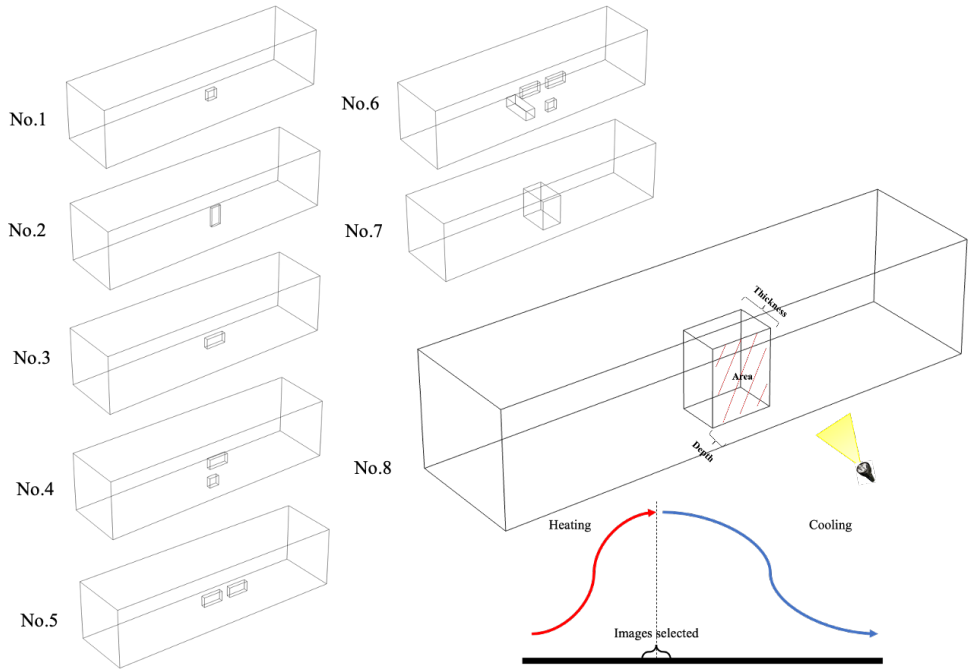

Figure 2. Concrete sample and test procedure.

Table 1. Size of subsurface delamination.

Sample No.	Width/mm	Length/mm	Thickness/mm
1	25	25	10
2	25	50	5
3	25	50	10
4	25	50	10
	25	25	10
5	25	50	10
	25	50	10
6	25	50	10
	25	50	10
	25	25	75
	25	25	10
7	50	75	75
8	75	100	50

2.3. Test Setup

In order to realize the damage density calculation and verification, an active thermography test was set up in lab to acquire the IR images from the concrete surface. The lab-scale experimental setup shown in Figure 3 was made of a real-time monitor, an IR thermal camera, a high-energy halogen torch, and concrete samples.

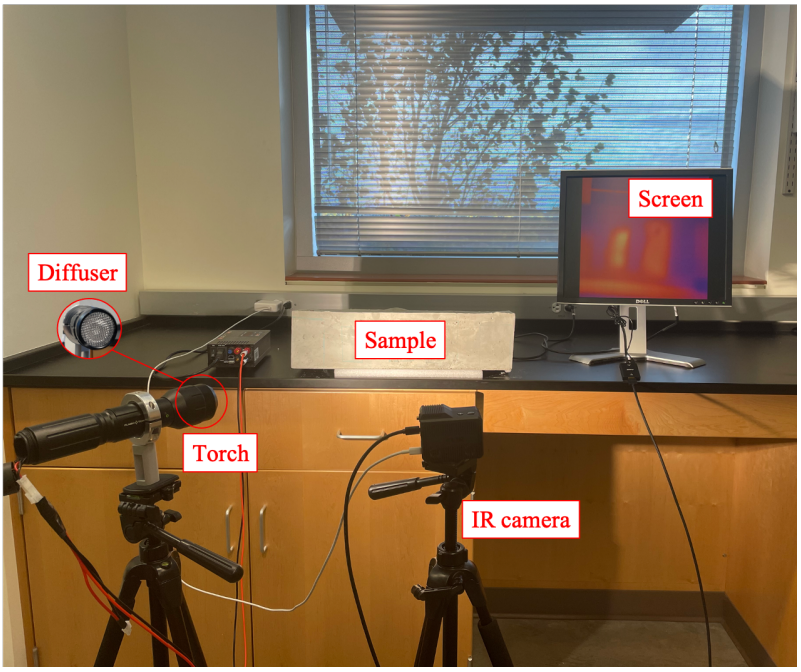

Figure 3. Test setup.

Activate heating input was provided from the front surface of the defect. A 100 W Halogen lamb was selected as a heat source excitation in this experiment because it is easy to be embedded into in situ testing equipment. In order to avoid uneven heat distribution, the lens of the torch was replaced by a diffuser, which can make the light uniformly distributed on the concrete surface. It is noteworthy that the main purpose of this lab setup was to determine the subsurface defects of different sizes, which would not be possible to be characterized by visual inspection methods [7–9]. Enabled by our high-fidelity simulations, experimental testing data collected during both the heating and cooling periods can be used to detect subsurface defects. Given that the subsurface defects have a significant difference in thermal conductivity and capacity, higher temperature occurs at the defect location, and then the heat flow reflects the sample surface. The heterogeneous temperature distribution captured by the IR camera can be correlated to subsurface defects. To accurately detect the temperature field, a FLIR Duo® Pro R 640 thermal camera (Uncooled Vox Microbolometer) was utilized to capture the IR thermal images of the specimens. While heating the surface, the area covering the defects inside the concrete specimen was considered a target area. The main characteristics of the IR camera are listed in Table 2.

Table 2. The main characteristics of the FLIR Duo® Pro R thermal camera.

Characters	Parameters
Measurement range	−20 °C to +50 °C
Spectral Band	7.5–13.5 µm
Thermal Sensitivity	<50 mK
Thermal Sensor Resolution	640 × 512
Thermal Frame Rate	30 Hz
FOV (field of view)	56°(H) × 45°(V)

To ensure efficient heating effects in the working condition, the distance between the sample surface and the thermal camera was set to 50 cm. The IR camera is placed on a tripod. In this way, the distance between the specimens and lens of the IR camera can be fixed accurately. The ambient temperature was set at 20 °C in the lab room, and the relative humidity was kept at 50 percent, which was maintained the same during the whole test procedure to reduce the influence from environmental impacts. The concrete surface was heated using the high-energy torch for 1 min, and later, it went through cooling for

3 min. A sequence of 480 frames was recorded at 0.5 s intervals by the thermal camera during the whole process. Raw data from the camera were processed at first using software, FLIR ResearchIR MAX, where the pixels' temporal temperature were converted to the third dimension. In order to make the result more robust, a series of images were selected in each test during the heating time and cooling time. Seven images were selected to test and verify at around the end of the heating phase for each of the tests as shown in Figure 2. This is because, around this stage, collected thermal data have better temperature contrast between the target and non-defect areas of concrete than any other time.

Given the instant heat transfer carried out within the concrete sample, heterogeneous temperature distribution can be easily observed from the surface in 1.5 min. Thus, active thermography is an easily accessible NDT approach for subsurface defects inspection. However, the collected raw IRT image data include a lot of noise which are introduced by ambient wind, moisture, and temperature variance and cannot be directly used for engineering inspection. Thus, to address this common concern, the engineering application-oriented thermography analytics approach was proposed to process the raw IR data, which is then followed by the damage density that directly links to infrastructure materials condition assessment.

2.4. Evaluation Metrics

In order to evaluate the performance of the proposed thermography analysis, evaluation metrics are needed to evaluate the subsurface defects detection accuracy. The SNR (Signal-to-noise ratio) index was widely used in the comparison of thermographic data processing methods and parameter optimization [16,26]. It was defined by the contrast between the target and non-defect areas. In field test, the most interested parameters when using IR images to detect subsurface delamination are the error in the considered area and the size prediction. Root mean square error (RMSE) was introduced to evaluate the overall detectability of defects in IR images. However, the RMSE indicator only cares about the area while the size, including the width and length, of the delamination is also quite significant in assessing the performance of IR image processing [16]. Therefore, a modified RMSE (mRMSE) was introduced in this paper. In this case, errors from the area as well as the width and length of the defect are taken into consideration. As shown in Equation (8), the smaller the mRMSE value, the smaller the difference between the real defects and estimated results:

$$mRMSE = \sqrt{\frac{\sum_{i=1}^{n}\left(\frac{|A_i-\hat{A}_i|}{A_i} + \frac{|W_i-\hat{W}_i|}{W_i} + \frac{|L_i-\hat{L}_i|}{L_i}\right)^2}{n}} \tag{8}$$

where A_i is the actual area of the ith defect, W_i is the actual width of the ith defect, L_i is the actual length of the ith defect, $\hat{A}_i$ is the predicted area of the ith defect in a processed image, $\hat{W}_i$ is the width of the minimum circumscribed rectangle of the ith defect in a processed image, $\hat{L}_i$ is the length of the minimum circumscribed rectangle of the ith defect in a processed image, and n is the number of defects in an image.

Values of $\hat{A}_i$, $\hat{W}_i$, and $\hat{L}_i$ can be easily calculated using Equations (9)–(11):

$$\hat{A}_i = \frac{A_{pixel}}{S^2} \tag{9}$$

$$\hat{W}_i = \frac{W_{pixel}}{S^2} \tag{10}$$

$$\hat{L}_i = \frac{L_{pixel}}{S^2} \tag{11}$$

where A_{pixel} is the area counted by pixels, W_{pixel} is the width counted by pixels, L_{pixel} is the length counted by pixels, and S is the scale between the image size and the real size. In this

work, the height of the concrete beam is 150 mm, while it occupies 414 pixels in the image. Thus, the number of pixels in each millimeter can be easily calculated as it is 2.76 pixels in 1 millimeter.

3. Results and Discussion

In order to figure out, which kind of image processing procedure best suits the damage density calculation, the image process methods were compared with each other. First, the raw data were obtained using the IR camera initially. Then, after cropping the ROI from the raw IR image, five preprocessing methods were applied to the original image including contrast adjustment, histogram equalization, and filters (Mean, Log, and Gaussian). After that, the modified OTSU algorithm was applied to the preprocessed images and morphology closing was utilized to fill in the gaps of the defects. Images after being processed by the preprocessing methods and the binary pictures after the closing operation of some tests are shown in Figure 4.

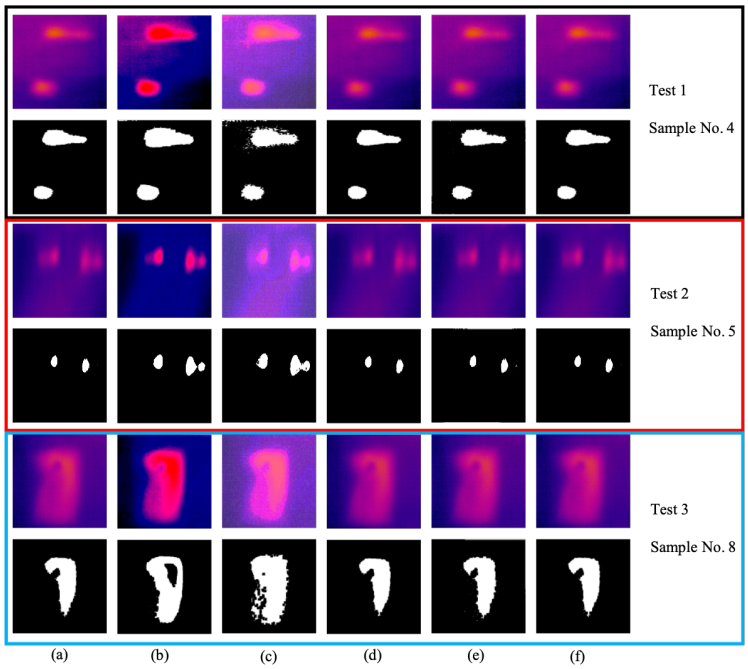

Figure 4. The results of preprocessing and binarized images: (**a**) Raw image; (**b**) Contrast adjustment; (**c**) Histogram equalization; (**d**) Mean filter; (**e**) Log filter; (**f**) Gaussian filter.

Three samples were selected in order to show the results from different preprocessing methods. The first two rows of images resulted from sample No. 4, the median two rows resulted from sample No. 5, and the last two rows of images are results from sample No. 8. The defects in Sample No. 4 and No. 5 have the same depth and number but different areas, while the defect in sample No. 8 has a deep depth and a larger area.

Based on the raw image, the results from images processed by the mean filter, Gaussian filter, and log filter did not show an apparent difference compared to the original image. However, it clearly showed that the contrast adjustment and histogram equalization made the defects higher detectability than the raw image in all three tests, as the segmented area shown in the binarized images are closer to the actual area. In addition, the segmented void area processed by the histogram equalization was more complete than others.

The mRMSE was used to compare the improvement between different image processing methods. The defects' area, width, and length of the minimum circumscribed rectangle of these defects were extracted to calculate the mRMSE value. The pixels in the clustered area are counted, as well as the width and length of the minimum circumscribed rectangle, which includes the detected defects. Then, Equation (8) was used to calculate the mRMSE values from different image process methods. RMSE which only took the area of the defects into consideration was compared with the proposed mRMSE method [16].

Figure 5 shows the mean values and standard deviation of these two methods in the tests described in Figure 4.

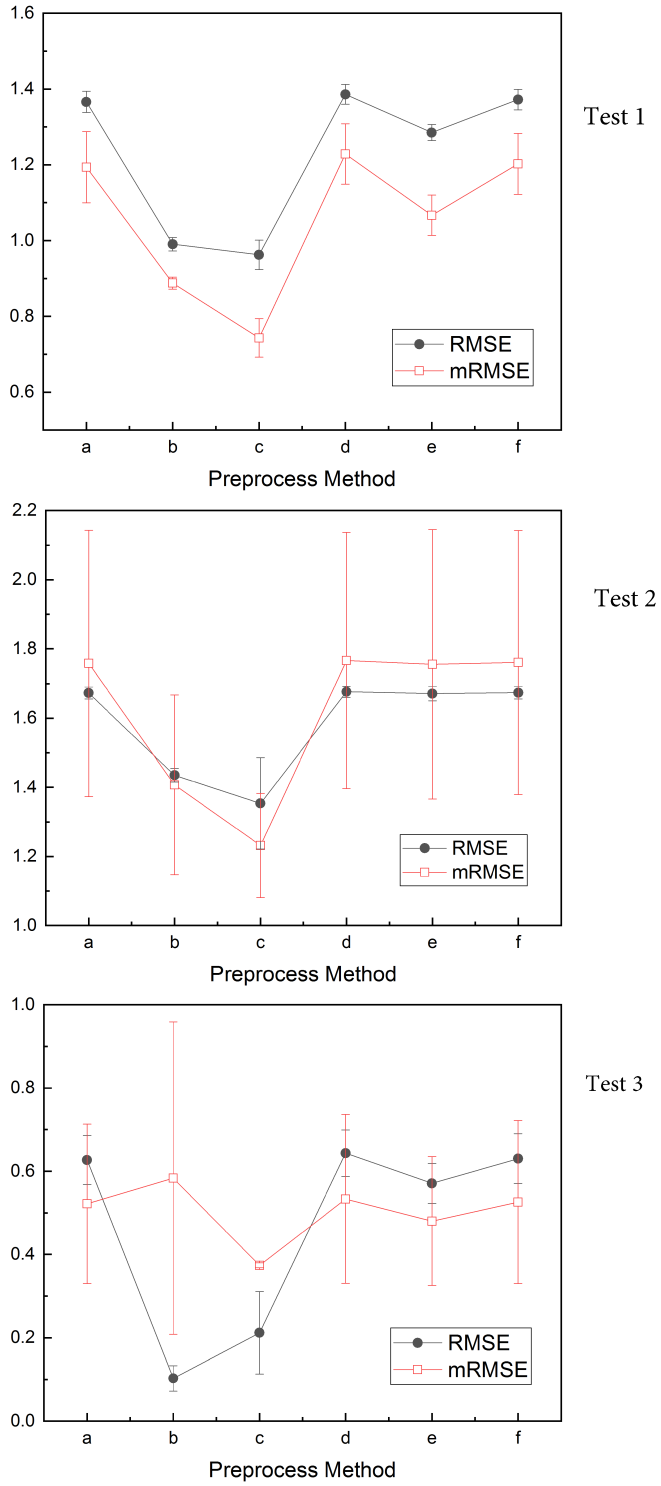

Figure 5. The result of mRMSE and RMSE value comparison for different preprocessed image in test 1, 2, and 3, respectively: (**a**) Raw image; (**b**) Contrast adjustment; (**c**) Histogram equalization; (**d**) Mean filter; (**e**) Log filter; (**f**) Gaussian filter.

It illustrated that, in different tests, the mean mRMSE is different with each other. It is mainly because that the area and size of the defects in each test are different while the calculation of mRMSE is based on these factors. However, in each test, the average

mRMSE value of the image processed by the histogram equalization is the lowest compared to other preprocessed images and the raw image. It means that histogram equalization makes the IR image more detectable as it caused the lowest detection error, which is consistent with the result from Figure 4. By comparing the RMSE and mRMSE methods, the standard deviation of mRMSE is larger than the RMSE, as the mRMSE takes the size of defects into consideration while the RMSE only calculates the area of the defects. In test 1 and test 2, the difference in the RMSE value between contrast adjustment and histogram equalization is lower than the difference in the mRMSE. In test 3, the RMSE of contrast adjustment is even lower than the histogram equalization. However, it is apparent that the histogram equalization detects the areal more accurate than contrast adjustment shown in Figure 4. It means that the proposed mRMSE in this work has a better ability to evaluate the performance of the IR image segmentation result.

After choosing the histogram equalization as the image preprocessing method, next step is to calculate the damage density index. The calculation of damage density for each concrete sample was based on the thermography analysis presented in Figure 1. Figure 6 shows the calculating results in each step of these eight experiments.

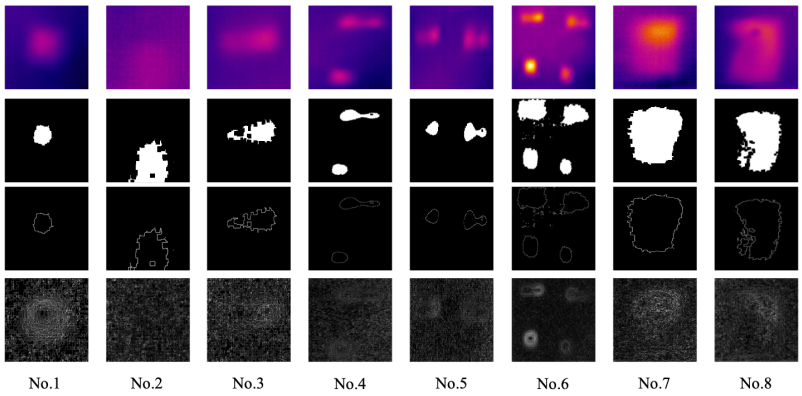

Figure 6. Calculating results in each step of the eight samples.

Each column in Figure 6 represents a single test for a corresponding concrete sample number. The first row is the original IR image from the eight samples. According to the proposed calculation framework, the second row is the binary images resulting from the image process method. Then, the gradient of the binary image was calculated to locate the edge of the subsurface defects as shown in the third row. A normalized temperature gradient map in the fourth row was generated through the original thermography, which shows the temperature's gradient distribution in the image. Using the location of the delamination's edge and the gradient map, the average gradient $\overline{\nabla}_i$ of the ith delamination can be obtained, and eventually, the damage density index can be calculated using Equation (1). The mean and standard deviation of the damage density from each test was calculated and shown in Figure 7.

To describe the damage intensity and distribution of infrastructures using the damage density index, the condition of the target area should be described so that the damage density index can be linked to the damage condition. In this work, the volume of Styrofoam was defined as a metric to show how severe the subsurface void's condition is in concrete samples. This is because all the Styrofoam blocks are buried at the same depth (5 mm), the only difference is the number and size of these defects. A larger volume of voids means a worse condition of the sample. Therefore, in order to describe each sample's damage condition, volume becomes the best index.

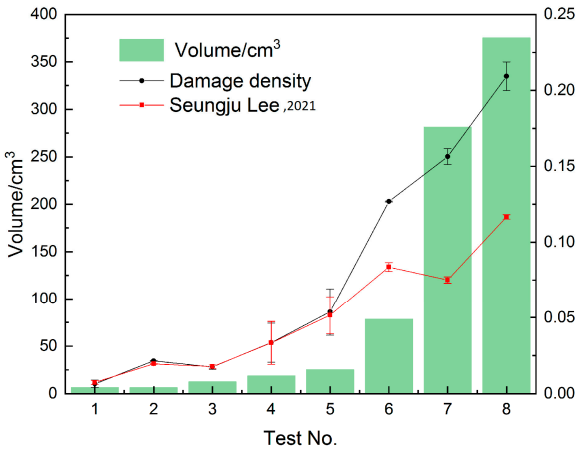

Figure 7. The plot of damage density and volume of defects [16].

Both the damage density and volumes of voids represent the damage condition of the target area. Thus, if the damage density shows a good relationship with the volume of the voids, that means the damage index can depict the target's condition well. The relationship between the volume of voids and the damage density of each sample was plotted in Figure 7. The green color bar represents the volume of the real subsurface voids in each test. The black point represents the calculated damage density in each experiment. The results from a traditional method described in Lee's paper, which only segmented the area and did not care about the severe degree of each defect, was compared with the damage density [16]. As we can see from Figure 7, in the tests from No. 1 to No. 5, the traditional image segmentation method was consistent with the damage density result. This is mainly because, in the first five samples, their thicknesses are all 10 mm (only the thickness of the defect in test No. 2 is 5 mm). Thus, there is not much difference between the proposed index and Lee's method. However, in the test No. 6, No. 7, and No. 8, the results from Lee's method are not consistent with the volume of the defects. This is because the thickness of the defects varies, and Lee's method could only catch the change in the area. Thus, Lee's method could not represent the damage condition of the samples well.

As for the damage density, its value did not strictly follow the volume change pattern of the defects, such as test No. 1 and No. 2. It happens mainly due to the variance from the ambient temperature, the system error, and the heterogeneity in materials when mixing. However, generally, it still shows that the damage density and volume of the voids in the concrete samples have a positive linear relationship. Thus, linear regression was applied between damage density and the volume of the subsurface voids. The Pearson correlation coefficient is around 0.94, which confirms that they are in a good linear relationship. It means that the damage density index can represent the damage intensity of total subsurface delamination in the inspected infrastructure.

4. Conclusions

In this work, a damage-index-based method for the quick evaluation of civil infrastructure using thermography analytics was proposed to improve the utility and interpretability of the IRT, leading to automated analysis and quantitative evaluation. The main contents can be concluded as follows:

1. The mRMSE is the first-ever developed metric in this work as an effort to evaluate the performance of different image-processing methods. Compared to RMSE, the mRMSE, which gives the size, the same significance as area, can reflect the prediction error more precisely.
2. A thermography-analytics-based framework, including IR image processing, image gradient calculating, and defects' edge detection, was proposed to calculate the damage density index which emphasizes both the area and the gradient of defects.

3. During image preprocessing, five image preprocessing methods were compared using the average mRMSE value to optimize the performance of the whole image process. Among these methods, histogram equalization was selected as the best preprocessing method because of its lower mRMSE value than the other methods.
4. After preprocessing, IR images were segmented by a modified OTSU algorithm because the concrete IR images with subsurface delamination are heavily skewed in the gray-level histogram. This modified OTSU algorithm uses the median value to replace mean value to reduce the influence of the asymmetric gray level. The closing was utilized to perform as a second denoising step. It can combine the separate defect parts after segmentation as a whole, which can improve the precision of the final result.
5. After running several samples in this research, it was shown that the index damage density has a positive linear relationship (the correlation coefficient is 0.94) with total volumes of the subsurface voids in the detection area compared to traditional image segmentation methods. As the volume of the subsurface voids represents the damage condition in field inspection, a numerical correlation between the damage density and damage condition in the infrastructure was determined.

As such, there is a high potential of utilizing this developed thermography analytics method of this work in the subsurface defect detection of concrete structures. By using this method, it is operational efficiency for engineers to quantitatively evaluate the conditions of civil infrastructures as engineers only need to take pictures from the infrastructure surface. Then, all the processing works would be carried out by the presented framework without any other calculation or signal analysis, which is a must in other non-destructive detection methods, such as GPR (Ground Penetrating Radar) or Ultra-sound device.

5. Next Steps and Future Research

For future engineering practice, more samples should be casted to figure out the robustness and accuracy of the damage density calculation framework.

In the lab experiment, the subsurface voids' volume was utilized to represent the damage it could cause to the infrastructure. However, in field testing, there exist many subsurface defects in civil infrastructure. Thus, the volumes of defects may not be able to represent the damage condition of the inspecting area. The defect's material, depth, and whether it is located in the key part of a infrastructure also play significant roles. Therefore, when applying the damage density to in situ detection, for each kind of subsurface defects, damage density calculation equation should be changed according to the experimental experience. For example, add some coefficients to the damage density calculation equation, such as disease-type coefficient, depth coefficient, or importance coefficient, etc.

Author Contributions: Conceptualization, Y.L. and T.Z.; methodology, T.Z. and A.P.; software, T.Z.; validation, T.Z., M.A.R. and Y.L.; formal analysis, T.Z. and A.P.; investigation, Y.L.; resources, Y.L.; data curation, T.Z.; writing—original draft preparation, T.Z.; writing—review and editing, Y.L. and M.A.R.; visualization, T.Z.; supervision, Y.L.; project administration, Y.L.; funding acquisition, Y.L. All authors have read and agreed to the published version of the manuscript.

Funding: This work was supported by the Idaho Department of Commerce (Grant # 003952).

Institutional Review Board Statement: Not applicable.

Informed Consent Statement: Not applicable.

Data Availability Statement: The data presented in this study are openly available. Nevertheless, it is possible to contact one of the study authors.

Acknowledgments: Constructive discussions with Zach Adams from Pitch Aeronautics are greatly appreciated.

Conflicts of Interest: The authors declare no conflict of interest.

References

1. Omar, T.; Nehdi, M.L. Remote sensing of concrete bridge decks using unmanned aerial vehicle infrared thermography. *Autom. Constr.* **2017**, *83*, 360–371. [CrossRef]
2. Omar, T.; Nehdi, M.L. Non-Destructive testing of bridge deck using passive infrared thermography and ground penetrating radar. In Proceedings of the 2016 Conference of the Transportation Association, Toronto, ON, Canada, 25–28 September 2016 .
3. Pozzer, S.; Rosa, F.D.; Pravia, Z.; Azar, E.R.; Maldague, X. Long-Term Numerical Analysis of Subsurface Delamination Detection in Concrete Slabs via Infrared Thermography. *Appl. Sci.* **2021**, *11*, 4323. [CrossRef]
4. Tran, Q.H.; Han, D.; Kang, C.; Haldar, A.; Huh, J. Effects of Ambient Temperature and Relative Humidity on Subsurface Defect Detection in Concrete Structures by Active Thermal Imaging. *Sensors* **2017**, *17*, 1718. [CrossRef] [PubMed]
5. Milovanović, B.; Gaši, M.; Gumbarević, S. Principal component thermography for defect detection in concrete. *Sensors* **2020**, *20*, 3891. [CrossRef] [PubMed]
6. Jang, K.; An, Y.K. Multiple crack evaluation on concrete using a line laser thermography scanning system. *Smart Struct. Syst.* **2018**, *22*, 201–207.
7. Golrokh, A.J.; Lu, Y. An experimental study of the effects of climate conditions on thermography and pavement assessment. *Int. J. Pavement Eng.* **2019**, *22*, 1030–1041. [CrossRef]
8. Golrokh, A.J.; Gu, X.; Lu, Y. Real-Time Thermal Imaging-Based System for Asphalt Pavement Surface Distress Inspection and 3D Crack Profiling. *J. Perform. Constr. Facil.* **2021**, *35*, 04020143. [CrossRef]
9. Lu, Y.; Golrokh, A.J.; Islam, A. Concrete Pavement Service Condition Assessment Using Infrared Thermography. *Adv. Mater. Sci. Eng.* **2017**, *2017*, 3829340. [CrossRef]
10. Meola, C. Infrared Thermography in the Architectural Field. *Sci. World J.* **2013**, *2013*, 323948. [CrossRef]
11. Khatereh, V. *Infrared Thermography Enhancements for Concrete Bridge Evaluation*; Michigan Technological University: Houghton, MI, USA, 2013.
12. Huh, J.; Mac, V.H.; Tran, Q.H.; Lee, K.-Y.; Lee, J.-I.; Kang, C. Detectability of Delamination in Concrete Structure Using Active Infrared Thermography in Terms of Signal-to-Noise Ratio. *Appl. Sci.* **2018**, *8*, 1986. [CrossRef]
13. Shrestha, R.; Kim, W. Non-destructive testing and evaluation of materials using active thermography and enhancement of signal to noise ratio through data fusion. *Infrared Phys. Technol.* **2018**, *94*, 78–84. [CrossRef]
14. Hiasa, S.; Birgul, R.; Catbas, F.N. A data processing methodology for infrared thermography images of concrete bridges. *Comput. Struct.* **2017**, *190*, 205–218. [CrossRef]
15. Xu, C.; Xie, J.; Chen, G.; Huang, W. An infrared thermal image processing framework based on superpixel algorithm to detect cracks on metal surface. *Infrared Phys. Technol.* **2014**, *67*, 266–272. [CrossRef]
16. Lee, S.; Chung, Y.; Shrestha, R.; Kim, W. Automated Defect Detection Using Threshold Value Classification Based on Thermographic Inspection. *Appl. Sci.* **2021**, *11*, 7870. [CrossRef]
17. Cheng, C.; Shen, Z. The application of gray-scale level-set method in segmentation of concrete deck delamination using infrared images. *Constr. Build. Mater.* **2020**, *240*, 117974. [CrossRef]
18. Abdel-Qader, I.; Yohali, S.; Abudayyeh, O.; Yehia, S. Segmentation of thermal images for non-destructive evaluation of bridge decks. *NDT E Int.* **2008**, *41*, 395–405. [CrossRef]
19. Pozzer, S.; Rezazadeh Azar, E.; Dalla Rosa, F.; Chamberlain Pravia, Z.M. Semantic segmentation of defects in infrared thermographic images of highly damaged concrete structures. *J. Perform. Constr. Facil.* **2021**, *35*, 04020131. [CrossRef]
20. Farmaki, S.; Exarchos, D.A.; Tragazikis, I.K.; Matikas, T.E.; Dassios, K.G. A Novel Infrared Thermography Sensing Approach for Rapid, Quantitative Assessment of Damage in Aircraft Composites. *Sensors* **2020**, *20*, 4113. [CrossRef]
21. Hiasa, S.; Birgul, R.; Catbas, F.N. Effect of Defect Size on Subsurface Defect Detectability and Defect Depth Estimation for Concrete Structures by Infrared Thermography. *J. Nondestruct. Evaluation* **2017**, *36*, 57. [CrossRef]
22. Watase, A.; Birgul, R.; Hiasa, S.; Matsumoto, M.; Mitani, K.; Catbas, F.N. Practical identification of favorable time windows for infrared thermography for concrete bridge evaluation. *Constr. Build. Mater.* **2015**, *101*, 1016–1030. [CrossRef]
23. Grys, S. Determining the dimension of subsurface defects by active infrared thermography—Experimental research. *J. Sens. Sens. Syst.* **2018**, *7*, 153–160. [CrossRef]
24. Yang, X.; Shen, X.; Long, J.; Chen, H. An Improved Median-based Otsu Image Thresholding Algorithm. *AASRI Procedia* **2012**, *3*, 468–473. [CrossRef]
25. Zhan, Y.; Zhang, G. An Improved OTSU Algorithm Using Histogram Accumulation Moment for Ore Segmentation. *Symmetry* **2019**, *11*, 431. [CrossRef]
26. Liu, Y.; Liu, K.; Gao, Z.; Yao, Y.; Sfarra, S.; Zhang, H.; Maldague, X.P. Non-destructive defect evaluation of polymer composites via thermographic data analysis: A manifold learning method. *Infrared Phys. Technol.* **2019**, *97*, 300–308. [CrossRef]